

Probing elastic anisotropy of human skin in vivo with light using non-contact acoustic micro-tapping OCE and polarization-sensitive OCT

Mitchell A. Kirby

University of Washington

Peijun Tang

University of Washington

Hong-Cin Liou

University of Washington

Maju Kuriakose

University of Washington

John J. Pitre

University of Washington

Tam N. Pham

University of Washington

Russell Ettinger

University of Washington

Ruikang K. Wang

University of Washington

Matthew O'Donnell

University of Washington

Ivan Pelivanov (✉ ivanp3@uw.edu)

University of Washington

Research Article

Keywords:

Posted Date: January 25th, 2022

DOI: <https://doi.org/10.21203/rs.3.rs-913561/v2>

License:   This work is licensed under a Creative Commons Attribution 4.0 International License.

[Read Full License](#)

Version of Record: A version of this preprint was published at Scientific Reports on March 10th, 2022. See the published version at <https://doi.org/10.1038/s41598-022-07775-3>.

1 **Probing elastic anisotropy of human skin in vivo with light using non-contact**
2 **acoustic micro-tapping OCE and polarization-sensitive OCT**

3 *Mitchell A. Kirby¹, Peijun Tang¹, Hong-Cin Liou¹, Maju Kuriakose¹, John J. Pitre Jr.¹, Tam N.*
4 *Pham², Russell Ettinger², Ruikang K. Wang¹, Matthew O'Donnell¹, and Ivan Pelivanov^{1*}*
5

6 ¹. University of Washington, Department of Bioengineering, Seattle, Washington, United States

7 ². University of Washington, Harborview Medical Center, Seattle, Washington, United States
8

9 **Abstract**

10 Skin broadly protects the human body from undesired factors such as ultraviolet radiation and
11 abrasion and helps conserve body temperature and hydration. Skin's elasticity and its level of
12 anisotropy are key to its aesthetics and function. Currently, however, treatment success is often
13 speculative and subjective, and is rarely based on skin's elastic properties because there is no
14 fast and accurate non-contact method for imaging of skin's elasticity. Here we report on a non-
15 contact and non-invasive method to image and characterize skin's elastic anisotropy. It combines
16 acoustic micro-tapping optical coherence elastography (A μ T-OCE) with a nearly incompressible
17 transversely isotropic (NITI) model to quantify skin's elastic moduli. In addition, skin sites were
18 imaged with polarization sensitive optical coherence tomography (PS-OCT) to help define the
19 fiber orientation. Forearm skin areas were investigated in five volunteers. Results clearly
20 demonstrate elastic anisotropy of skin in all subjects. A μ T-OCE has distinct advantage over
21 competitive techniques because it provides objective, quantitative characterization of skin's
22 elasticity without contact, which opens the door for broad translation into clinical use. Finally,
23 we demonstrate that a combination of multiple OCT modalities (structural OCT, OCT
24 angiography, PS-OCT and A μ T-OCE) may provide rich information about skin and can be used to
25 characterize scarring.
26

27 **Introduction**
28

29 Skin is a complex organ providing a broad spectrum of functions. Its biomechanical properties
30 may depend on environment (such as temperature and humidity), age, gender, body mass index,
31 skin thickness and body site, and any alteration of these properties may indicate disease ¹⁻⁷.
32

33 Reconstructive surgeries drive the clinical need for non-contact objective measurements of skin
34 elasticity. Skin grafts, including both split thickness and full thickness grafts (STSG or FTSG,
35 respectively), are indispensable techniques to manage complex burn injury, soft tissue injuries,
36 as well as secondary reconstructions. Pathological skin healing is characterized by hypertrophic
37 scarring, whereby thickened and fibrotic tissue cause disfigurement, contractures, and impaired
38 function in survivors. In 2018, there were 17.7 million aesthetic, 1.8 million aesthetic surgical,
39 15.9 million aesthetic minimally invasive and 5.8 million reconstructive procedures in the United
40 States alone, with a large fraction of interventions involving STSG or FTSG ⁸. Skin grafting is one
41 of the oldest and most widely applied reconstructive techniques, finding clinical applications
42 across primary and secondary burn reconstruction, trauma reconstruction, skin oncologic

43 surgery, and many areas of wound care including diabetic foot wounds, venous stasis ulcers,
44 pressure sores, and surgical wounds with delayed healing⁹⁻¹¹.

45
46 FTSG is generally used for aesthetically sensitive parts of the body, such as head and neck regions,
47 and involves harvesting the epidermis with the entire dermis at the subcutaneous/dermal
48 junction from the donor site. FTSG provides improved texture, pliability, elasticity, aesthetics,
49 color match and is more resistant to secondary contracture compared with STSG. FTSG is a
50 sensitive technique requiring multiple steps: donor skin harvest and primary donor site closure,
51 recipient site preparation, graft placement and securement, graft immobilization, and long-term
52 postoperative care and monitoring as the graft undergoes the standard phases of wound healing
53 including inflammatory (4-6 days), proliferative (up to three months) and remodeling (up to a
54 year or year and a half) phases^{10,11}.

55
56 A skin graft's functional and mechanical properties must be matched with surrounding recipient
57 tissue to restore both form and function and minimize scar. This is especially true for FTSG
58 surgery undertaken in the face or neck. Recent studies suggest that tissue elasticity is a critically
59 important parameter driving reconstructive success^{12,13}. Indeed, collagen fibers mainly
60 determine Young's modulus and elastic anisotropy (Langer's lines). Although medical providers
61 have long recognized that linear surgical incisions placed along Langer's lines heal with less
62 tension and scarring, it remains unclear how to best leverage elastic anisotropy when replacing
63 larger defects through skin grafting. Thus, STSG and FTSG's functional and aesthetic results will
64 be severely limited without matching the elasticity of adjacent recipient tissue¹⁴⁻¹⁶. Currently,
65 there are no non-contact methods to monitor skin elastic properties, especially its anisotropy.

66
67 Recently, optical coherence elastography (OCE) was proposed to remove the last drawback in
68 shear wave elastography, i.e., to make this method fully non-contact¹⁷. Although static and
69 vibrational OCE still require tissue contact, dynamic OCE does not require it at all. Indeed, in 2016,
70 air-coupled ultrasound was proposed to launch sub-mm wavelength propagating mechanical
71 waves in tissue via reflection-based acoustic radiation force¹⁸. This acoustic micro-tapping
72 method ($A\mu T$) was combined with phase-sensitive OCT to create a fully non-contact method
73 ($A\mu T$ -OCE) of elasticity imaging in tissues¹⁹.

74
75 Despite the remarkable success in imaging propagating mechanical waves *in vivo* in cornea and
76 skin with $A\mu T$ -OCE, interpreting results and converting wave fields into elastic moduli has been
77 unclear for some time. Indeed, both cornea and skin are anisotropic, bounded, layered media.
78 Wave propagation in such media is complicated and reconstructing elastic moduli using surface-
79 propagating mechanical waves is not trivial. As such, an appropriate mechanical model is needed
80 to solve this problem. Recently, we developed a model of a nearly incompressible transversely
81 isotropic (NITI) medium²⁰, opening the way for quantitative evaluation of anisotropic elastic
82 properties in biological tissues. We used the NITI model to quantify corneal elasticity and justified
83 it by direct comparison with mechanical tests²¹.

84
85 Numerous mechanical tests have evaluated the elastic behavior of skin, including indentation,
86 torsion, tension, and suction²²⁻²⁶; corresponding tools were commercialized (Dermaflex²⁷ and

87 Cutometer²⁸). All such methods have similar disadvantages. Most use simple linear stress-strain
88 relationships, depend on tip geometry, ignore skin's multilayered structure and anisotropy, do
89 not account for skin thickness, and require contact. Although they are occasionally used in
90 dermatology, contact tests are not currently used to monitor plastic and burn surgeries, and skin
91 graft outcomes, because physical contact produces considerable patient discomfort and
92 measurements are not sufficiently objective or reproducible to guide clinical decision making²⁷.

93
94 Young's moduli of skin reported in the literature demonstrate dramatic variations depending on
95 the measurement technique²⁹. The range of moduli reported from indentation tests is usually
96 from Pa to tens of kPa³⁰⁻³², with great variability depending on the probe size used³³; suction
97 tests report values about hundreds of kPa³⁴⁻³⁶; torsion tests find Young's moduli on the order of
98 MPa³⁷⁻³⁸; and tensile measurements sometimes report values of hundreds of MPa for the
99 Young's modulus in skin³⁹⁻⁴¹. Thus, six orders of magnitude difference in Young's modulus can be
100 found in the literature.

101
102 An additional complication in characterizing skin's elasticity is its non-linearity, i.e., elastic moduli
103 depend on the tensile or deformation applied during measurements. The larger the deformation
104 applied, the larger the Young's modulus usually measured^{29, 33}. This is why low-deformation
105 methods are of critical importance to characterize skin under normal, physiologic conditions that
106 do not modify the object during measurement.

107
108 Current tools to evaluate scar longitudinally include the Vancouver Scar Scale (VSS) and the
109 Patient and Observer Scar Assessment Scale (POSAS)⁴². They include assessment of parameters
110 such as pliability, firmness, color, perfusion, thickness, and 3-dimensional topography. While
111 validated, they are both subject to observation bias and cannot quantitatively evaluate changes
112 within scar tissue.

113
114 Acoustic elastography is a low-deformation method using propagating mechanical waves to
115 probe tissue elasticity. Their excitation and detection can be done in different ways. Originally, a
116 mechanical vibrator in direct contact with tissue produced transient displacements⁴³; later, the
117 vibrator was replaced by acoustic radiation force generated by a focused ultrasound (US) beam⁴⁴,
118⁴⁵. Note that shear wave elastography has evolved into an indispensable clinical tool, especially
119 for the liver and breast^{46, 47}. However, shear wave elastography has not significantly impacted
120 clinical applications in skin even though multiple studies have been published. The main reason
121 is that US coupling material must be applied to the skin surface, representing a significant site of
122 contact; in addition, US coupling changes skin's hydration and is not ideal for burns and grafts.

123
124 The mechanical model is critically important to reconstruct material mechanical moduli from
125 experimental data (including methods using wave propagation). Reconstructed moduli can then
126 be used in a computational model to predict tissue deformation based on applied loads. Soft
127 biological tissues are nearly incompressible⁴⁸. If the medium is also isotropic, there is only one
128 parameter (shear modulus μ) defining both shear and tensile deformations; the Poisson's ratio
129 approaches 0.5 and the Young's modulus is $E = 3\mu$. Thus, μ is the sole parameter defining the
130 deformation of a linear, isotropic, incompressible elastic material.

131
132 Unfortunately, skin is not isotropic^{49,50}. The simplest model accounting for skin's anisotropy is
133 transversal isotropy (TI) with a symmetry axis defined by Langer's lines, i.e., fiber orientation. For
134 a nearly incompressible transversely isotropic (NITI) material (see Results and Supplementary
135 Notes), an additional shear modulus G and parameter δ are needed along with μ to describe
136 shear and tensile deformations in different directions relative to Langer's lines.

137
138 In this study, we further develop the NITI model²⁰ (recently introduced for cornea) for skin-type
139 material anisotropy, considering it as a locally transverse isotropic material with a symmetry axis
140 defined by Langer's lines. We used an A μ T-OCE system to image propagating waves along skin's
141 surface in human forearm *in vivo* in five healthy volunteers. For each subject, we varied the
142 Rayleigh (surface) wave propagation direction relative to Langer's lines and reconstructed all
143 three independent shear moduli. A μ T-OCE measurements can also define the material symmetry
144 axis, but it is desirable to measure the fiber orientation in skin independently to improve
145 reconstruction accuracy.

146
147 An independent measurement of skin's optic axis (or birefringence axis) was performed with
148 polarization-sensitive OCT (PS-OCT)⁵¹. Both A μ T-OCE and PS-OCT measurements revealed very
149 similar orientation of the symmetry axis in the epidermis for all measured subjects. To our
150 knowledge, non-contact quantitative evaluation of skin's elasticity and its anisotropy, with the
151 symmetry axis confirmed by independent PS-OCT measurements, has not been demonstrated
152 before. In addition, we present pilot results on imaging scar *in vivo* and show that rich information
153 can be obtained non-invasively with four different OCT modalities (structural OCT, OCTa, OCE
154 and PS-OCT). Combining measurements from these modalities can provide comprehensive
155 quantitative characterization of skin and pave the way for large-scale clinical studies in the future.
156

157 **Results**

158 **Nearly incompressible transverse isotropy (NITI) of skin's elasticity**

159 Dynamic OCE uses three principal steps: (i) excite propagating mechanical waves (surface waves
160 in our case), (ii) track propagating mechanical waves with phase sensitive OCT and (iii) reconstruct
161 tissue moduli from surface wave fields using a mechanical model. Even if the first two steps are
162 done properly, an inappropriate model will produce an incorrect reconstruction of medium
163 mechanical properties.

164 An example of the importance of using a correct mechanical model can be found in OCE applied
165 to the cornea, where the literature reported orders of magnitude mismatch in corneal elasticity
166 obtained with OCE compared to that measured with mechanical tensile tests. Originally, the
167 cornea was incorrectly considered an isotropic material. With the recent introduction of the
168 appropriate NITI model, reconstructed moduli closely match those measured with conventional
169 destructive mechanical tests. Indeed, the random in-plane orientation of corneal lamellae
170 supports the assumption of in-plane isotropy, but very different mechanical behavior out-of-

171 plane. Thus, at least two independent moduli must be considered for cornea. Further details on
 172 how corneal anisotropy influences wave behavior and affects moduli reconstruction can be found
 173 in Ref ²⁰.

174 We believe a similar approach must also be used for skin. In other words, skin's mechanical
 175 anisotropy must be taken into account. Indeed, Langer's lines define the primary orientation of
 176 fibers in skin. Although a fraction of collagen fibers may be oriented perpendicular to Langer's
 177 lines and some by 45 degrees, the majority are oriented along this direction ^{52, 53}. It means that,
 178 macroscopically, skin should behave as a NITI medium with a symmetry axis (Z-axis) associated
 179 with Langer's lines.

180 We start our description of a model for skin's elasticity with a general form of the elastic modulus
 181 matrix for a transversely isotropic (TI) material:

$$182 \quad C = \begin{bmatrix} C_{11} & C_{12} & C_{13} & & & \\ C_{12} & C_{11} & C_{13} & & & \\ C_{13} & C_{13} & C_{33} & & & \\ & & & C_{44} & & \\ & & & & C_{44} & \\ & & & & & C_{66} \end{bmatrix}, \quad (1)$$

183 where $C_{12} = C_{11} - 2C_{66}$ due to symmetry conditions. Since one principal plane in the TI material
 184 is isotropic, we use the conventional notation of an isotropic material with a few TI
 185 modifications ⁴⁸:

$$186 \quad C = \begin{bmatrix} \lambda + 2\mu & \lambda & \lambda + Q_1 & & & \\ \lambda & \lambda + 2\mu & \lambda + Q_1 & & & \\ \lambda + Q_1 & \lambda + Q_1 & \lambda + 2\mu + Q_2 & & & \\ & & & G & & \\ & & & & G & \\ & & & & & \mu \end{bmatrix}, \quad (2)$$

187 where λ and μ are the conventional Lamé constants. An additional modulus G shows that shear
 188 deformation can be different if shear stress is applied along the symmetry axis z compared to
 189 that applied across it. Modulus G can be very different from μ in soft tissue. In cornea, for
 190 instance, μ/G can be more than a hundred ²⁰.

191 Tensile deformations include the additional parameters Q_1 and Q_2 . Soft biological tissue is nearly
 192 incompressible so that shear moduli are many orders of magnitude smaller than longitudinal
 193 ones and therefore

$$194 \quad Q_1, Q_2 \sim \mu \ll \lambda. \quad (3)$$

195 Nevertheless, these small parameters are important in characterizing Young's moduli along, E_L ,
 196 and across, E_T , fibers, i.e., assuming that tensional deformation is different along the fiber
 197 direction compared to that across it.

198 In the isotropic, incompressible limit, $\mu = G$, Young's modulus $E_L = E_T = 3\mu$, and Poisson's ratio
 199 $\nu = 1/2$, i.e., both tensile and shear deformations can be characterized by a single parameter μ .

200 In Supplementary Note 1 we show how Young's moduli E_L and E_T , and Poisson's ratios are
 201 defined through Q_1, Q_2 and μ and how different they can be from 3μ for the skin-type NITI
 202 material. In summary, these important parameters can be written as (see Supplementary
 203 Note 1):

$$\begin{aligned}
 E_T &= 3\mu + \mu \left[\frac{\delta}{4\mu + \delta} \right], \\
 E_L &= 3\mu + \delta, \\
 \nu_{TT} &= \frac{1}{2} \left[1 + \frac{\delta}{4\mu + \delta} \right] = 1 - \frac{1}{2} \frac{E_T}{E_L}, \\
 \nu_{TL} &= \frac{1}{2} \left[1 - \frac{\delta}{4\mu + \delta} \right] = \frac{1}{2} \frac{E_T}{E_L}, \\
 \nu_{LT} &= \frac{1}{2},
 \end{aligned} \tag{4}$$

205 A few important observations can be drawn from these expressions: (i) Compared to the isotropic
 206 case, there are two parameters: μ and an additional parameter $\delta = Q_2 - 2Q_1$ that define the
 207 Young's moduli and Poisson's ratios. (ii) All Young's moduli and Poisson's ratios do not depend
 208 on the shear modulus G . (iii) The fact that ν_{LT} is equal to $1/2$ means that the deformation will be
 209 distributed equally in the isotropy plane when the stress is applied along the symmetry axis. (iv)
 210 However, when the stress is applied perpendicular to the fiber direction, the deformation will be
 211 distributed unequally along and perpendicular to the fibers, but the sum of them is equal to unit:

$$\nu_{TT} + \nu_{TL} = 1. \tag{5}$$

213 (v) The fact that $\nu_{TT} > 0$ imposes limitations on the relationship between E_L and E_T and their
 214 absolute values:

$$\begin{aligned}
 E_L &> E_T/2 \\
 E_L &> \mu \\
 E_T &> 2\mu
 \end{aligned} \tag{6}$$

216 Thus, there are three parameters primarily describing simple tensile and shear mechanical
 217 properties in the skin-type NITI material: μ , $\delta = Q_2 - 2Q_1$, and G .

218 Supplementary Figure 1 shows how Young’s moduli can change with δ . Clearly, E_T has a very
219 narrow range, with a lower limit of 2μ and upper limit of 4μ as $\delta \rightarrow \infty$. E_L is a linear function of
220 δ .

221 Since all Poisson’s ratios should be greater than 0 for normal materials, this further narrows the
222 range of E_T to

$$223 \quad 3\mu < E_T < 4\mu . \quad (7)$$

224 In practice, E_L is usually larger than E_T (Young’s modulus along fibers is larger than that across),
225 and the ratio of moduli is also usually limited by a factor $E_L/E_T < \sim 2$ ^{49,50}, i.e., $E_L < \sim 7\mu$.

226 Note that the skin is a multi-layered medium composed of epidermis, dermis, and hypodermis
227 (subcutaneous tissue). The outermost epidermal layer acts as a barrier but does not greatly affect
228 skin’s elastic behavior because it is very thin ($\sim 150 \mu\text{m}$). The deepest layer, hypodermis, connects
229 skin to muscles and acts mostly like a mechanical damping layer combined with thermal
230 insulation. Because subcutaneous tissue contains less fiber and more fat, its elasticity is much
231 smaller than that of dermis. The central layer, dermis, consists of elastin and collagen fibers that
232 account for about ninety percent of skin’s weight, and defines most of the mechanical elasticity
233 and anisotropy in skin⁵⁴. Thus, dermis is of primary interest.

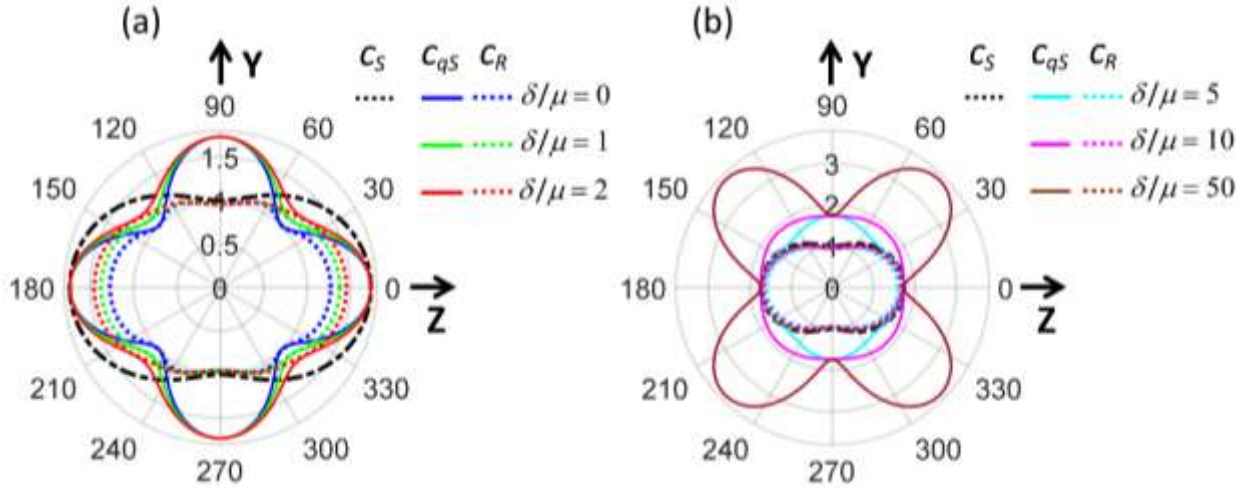
234 Uniaxial tensile and inflation tests yield Young’s modulus estimates related to μ and δ . However,
235 shear torsional tests depend only on G . This decoupling of normal and shear deformations helps
236 explain the discrepancy between tensile/inflation test modulus estimates.

237 **Wave propagation in a NITI medium**

238 As discussed above, we assume that skin’s elastic properties are mostly driven by the dermis,
239 which can be described as a NITI material. A NITI medium supports three bulk waves—quasi-
240 longitudinal, quasi-shear, and shear. Soft tissues are nearly incompressible ($\lambda \gg \mu$), implying that
241 the quasi-longitudinal wave speed is nearly constant along all directions. However, quasi-shear
242 and shear wave speeds do vary with angle and depend on both G/μ and δ/μ (see Supplementary
243 Note 2)^{55, 56}. Thus, the measurement of angle-dependent anisotropy in shear and quasi-shear
244 wave propagation can be used for elastic moduli reconstruction in skin.

245 Directly monitoring bulk shear wave propagation in the dermis is problematic. Indeed, the
246 thickness of the dermis varies between 0.3 mm and 3 mm, and shear-wave propagation will be
247 guided. Although multiple studies were performed using conventional shear wave elastography
248 in skin⁵⁷⁻⁵⁹, only a few discussed anisotropy⁶⁰ and none (to our knowledge) considered the
249 influence of boundaries. Ignoring these factors can lead to serious errors in moduli reconstruction
250 due to strong frequency dispersion. In addition, accounting for an irregular and not well-defined
251 transition between dermis and hypodermis is not a simple task.

252 An alternate approach measures the anisotropy of surface waves (as it is done in dynamic OCE),
 253 i.e., waves propagating along the skin surface in different directions relative to Langer's lines. In
 254 Supplementary Note 3 we showed that a solution for the angular dependence of Rayleigh
 255 (surface) wave speed can be obtained using the Stroh formalism^{61, 62}.



256
 257 **Figure 1. Anisotropy of phase velocity for bulk shear (black dashed line), quasi-shear (solid lines) and**
 258 **surface Rayleigh (dotted lines) waves in a fast-axis NITI medium. (a) $\delta/\mu < 2$, (b) $\delta/\mu > 5$. In both panels**
 259 **$G/\mu = 3$.**

260 Figure 1 shows the Rayleigh wave velocity as a function of propagation angle in the YZ plane using
 261 the coordinate system defined in Supplementary Note 2 at different parameters G/μ and δ/μ ;
 262 the velocities of shear c_S and quasi-shear c_{qS} waves are also shown for reference. Note the
 263 fundamental difference between waves propagating through the volume of a NITI material and
 264 over its surface.

265 When the Rayleigh wave propagates perpendicular to the symmetry axis over the surface of a
 266 fast-axis NITI medium (i.e., in the case of $\delta/\mu > 0$ as it is defined in Supplementary Note 1), its
 267 speed ($c_R(\vartheta)$) is solely defined by μ and does not depend on G and δ , i.e., it equals that for the
 268 isotropic material:

269
$$c_R(\vartheta = 90^\circ) = 0.9553c_S(\vartheta = 90^\circ) = 0.9553\sqrt{\mu/\rho}, \quad (8)$$

270 However, when the Rayleigh wave propagates along the fibers, its speed is a function of all
 271 parameters G , μ and δ and cannot be represented in a simple form. The solution of the secular
 272 equation (S27) (See Supplementary Note 3) can be done numerically or using a combination of
 273 parameters in Eq. (S27) as shown by Abramowitz in Ref⁶³.

274 An interesting observation is that when δ is smaller than G (see Fig.1a), at $\vartheta = 45^\circ$, the Rayleigh
 275 wave speed

276
$$c_R(\vartheta = 45^\circ) \approx c_{qS}(\vartheta = 45^\circ) = \sqrt{\frac{\mu + \frac{\delta}{4}}{\rho}}, \quad (9)$$

277 does not depend on G .

278 Although the quasi-shear wave speed is not limited by $\sqrt{G/\rho}$ and can change broadly with δ , the
 279 Rayleigh wave speed in the NITI medium cannot exceed $\sqrt{G/\rho}$. This limit is reached when $\delta/\mu \rightarrow$
 280 ∞ (see Fig.1b). This fact limits the sensitivity of using Rayleigh waves to invert elastic moduli when
 281 $\delta/\mu > \sim 10$, where the Rayleigh wave speed approaches that of the shear wave (Fig.1b):

282
$$c_R\left(\vartheta, \frac{\delta}{\mu} > \sim 10\right) \approx c_S(\vartheta) = \sqrt{\frac{G \cos^2 \vartheta + \mu \sin^2 \vartheta}{\rho}}. \quad (10)$$

283 Fortunately, the anisotropy is not so strong for human skin^{49,50}. Because the Rayleigh wave speed
 284 is a unique function of parameters μ , G and δ , it can be used to reconstruct elastic properties in
 285 skin, i.e., skin's Young's moduli and Poisson's ratios outlined in Eqs. (4). Additional details on
 286 Rayleigh wave anisotropy can be found in Supplementary Note 3.

287 There may be complications, similar to that for bulk waves, because of limited dermal thickness
 288 and boundaries. This is a complex problem, in general, but it can be simplified by considering all
 289 scales carefully. Indeed, a thin, compared to the mechanical wavelength, bounding layer barely
 290 affects the surface wave speed (see Supplementary Note 4). Subcutaneous tissue should produce
 291 guided waves with the dispersion determined by both dermis and hypodermis properties (see
 292 Supplementary Note 5).

293 Surprisingly, surface wave guidance was not observed in our experiments. In addition, we
 294 performed auxiliary experiments in chicken drumsticks where we explored surface wave
 295 propagation for two situations. First, OCE experiments were performed in whole chicken
 296 drumsticks (see Supplementary Note 6) and no guided wave behavior was observed. Then, skin
 297 was removed from muscle and positioned on the top of water. In this case, clear guided wave
 298 behavior was recorded. Reconstruction of shear wave speed from the dispersion analysis of
 299 guided waves in excised skin yielded a similar value to that obtained from group velocity analysis
 300 for the whole chicken drumstick.

301 We assume that these results can be explained by two factors: (i) small differences in elastic
 302 properties between skin layers and (ii) an irregular transition between layers. Both factors make
 303 reflections from the skin/subcutaneous tissue interface inefficient, which strongly reduces
 304 guided behavior. Thus, mechanical wave propagation along the skin surface can be considered
 305 propagation along the surface of a bulk NITI medium.

306

307 Elastic anisotropy of skin in human forearm: in vivo measurement with A μ T-OCE

308 A spectral-domain OCT system with a 46.5 kHz A-line rate operating in MB-mode⁶⁴ was used to
309 track propagating mechanical waves over the skin surface in healthy human volunteers' forearms
310 in vivo. The study was performed in accordance with the University of Washington Institutional
311 Review Board (STUDY00012306). A detailed description of the system can be found in our
312 previous studies^{18-20, 64, 65}. Briefly, a cylindrically focused 1 MHz air-coupled ultrasound
313 transducer (A μ T) provided a spatially and temporally sharp push to the skin surface in the
314 investigated body site, generating mechanical waves with a bandwidth up to 4 kHz (see **Methods**
315 **Section**). For each human subject, measurements were performed at different propagation
316 angles relative to a chosen coordinate system. Because Langer's lines in the forearm are
317 traditionally described as orthogonal to the axial forearm direction, the coordinate system was
318 chosen as represented in Fig. 2a.

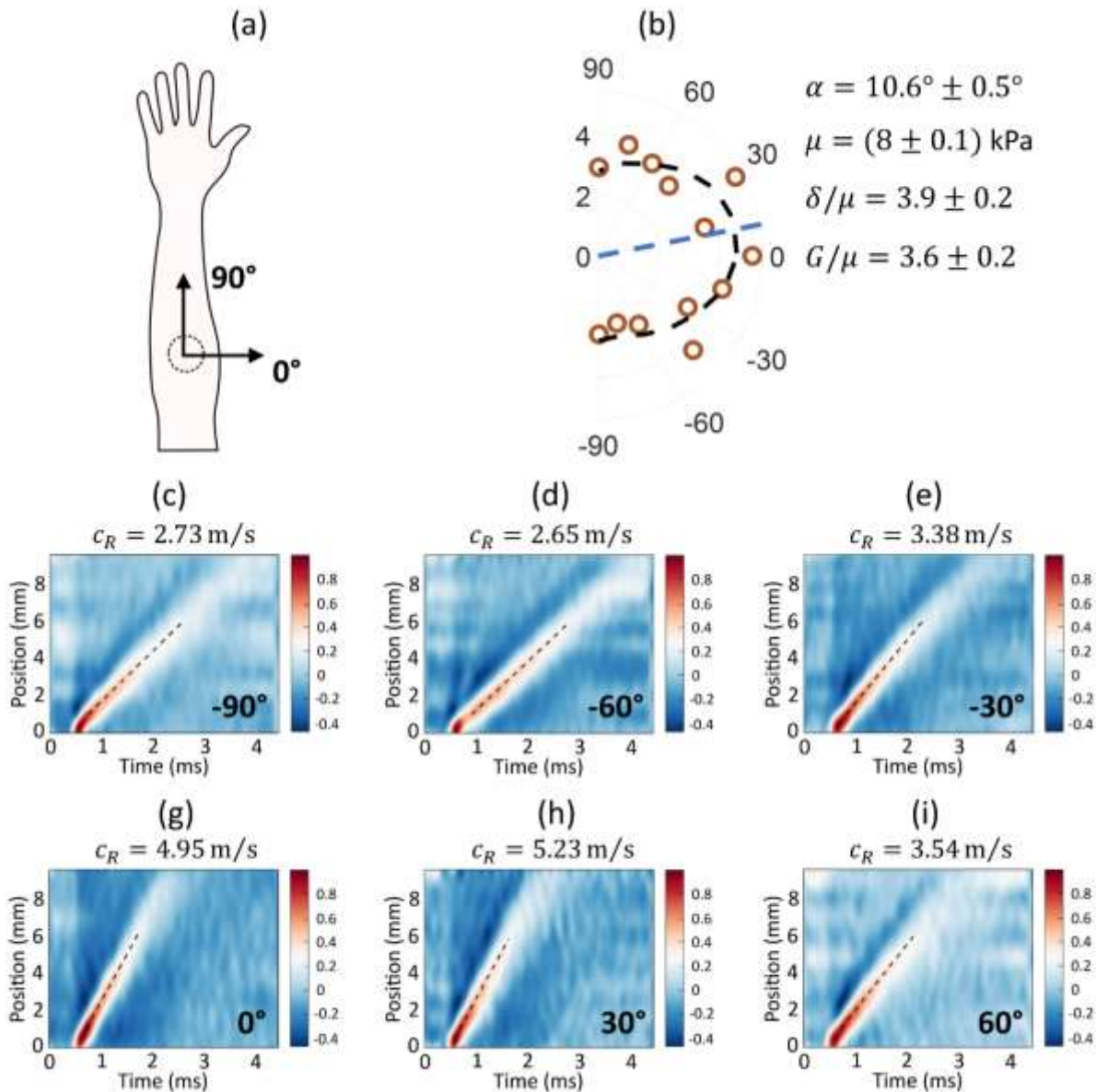
319 The anisotropy of surface wave group velocity measured with A μ T-OCE is presented in Fig. 2b
320 with dots. Individual wavefields (collection of signal profiles recorded at different distances from
321 the A μ T source) are presented in Figs. 2c-h for different propagation directions over the skin
322 surface. There were 13 datasets for each human subject corresponding to a range of propagation
323 directions between -90° and 90° with a step of 15°.

324 There are a few important observations from Figs. 2c-h. First, recorded wavefields do not look
325 dispersive as we observed previously in cornea²⁰ or in chicken skin placed on water (see
326 Supplementary Note 6). It means that subcutaneous tissue has little influence on surface-
327 propagating mechanical waves and the wave speed can be characterized with the group velocity.
328 For every propagating direction, we fit wavefields with a linear function; fitting results are shown
329 on the top of each panel in Figs. 2c-h and summarized in Fig. 2b for all propagation directions.
330 Second, the speed of surface waves is angle-dependent, which confirms that skin is elastically
331 anisotropic.

332 Fitting Rayleigh wave anisotropy with the theoretical function (see Fig. 1) can be used to extract
333 elastic moduli μ , G and δ , which can be used to calculate the tensile anisotropy (E_L/E_T) and shear
334 anisotropy (G/μ). We fit OCE data using four parameters, with the initial guess of the skin's actual
335 fiber orientation α relative to the classic orientation of Langer's line in the forearm (see Fig.3a).
336 To determine actual inaccuracies in estimated fit parameters, a 'Leave-one-out cross-validation'
337 method was used⁶⁶. A total of N-1 data points were used to fit the data N times, and the average
338 over N values produced estimates of the mean for all fit parameters.

339 For the subject (Subject #4) presented in Fig. 2b, the orientation of the mechanical axis, i.e.
340 Langer's lines, was determined to be $\alpha = 10.6^\circ \pm 0.5^\circ$. This value is not zero; that is, Langer's
341 lines are not exactly perpendicular to the axial forearm direction. Values for α , μ , δ/μ and G/μ
342 are shown in the right bottom corner of Fig. 2b. Clearly, skin anisotropy in the forearm is quite
343 strong for Subject #4. It means that tissue deformation across Langer's lines should be about 2
344 times greater than along them ($E_L/E_T = 1.98$) for the same applied one-dimensional load, which

345 is very important to know when planning graft placement, orientation and predicting secondary
 346 contractions from skin graft surgeries.



347

348 **Figure 2. An example of in-plane anisotropy of Rayleigh wave propagation in skin (forearm body area,**
 349 **Subject #4).** (a) Schematic of the measurement site. Imaging of propagating mechanical waves was
 350 performed with $\text{A}\mu\text{T-OCE}$ in different propagation directions in human forearm in vivo. Zero propagation
 351 angle ϑ corresponds to the direction perpendicular to the axial forearm direction, which corresponds to
 352 the direction of traditional Langer's lines. (b) Measured anisotropy of Rayleigh wave speed in Subject #4
 353 (dots) and the best fit to the analytic solution derived from the NITI model (see Supplementary Note 3).
 354 The defined orientation of the mechanical symmetry axis (Langer's lines) $\alpha = (10.6 \pm 0.5)^\circ$, and the shear
 355 modulus μ and anisotropy factors correspond to the values at minimum fit error. (c)-(i) Measured
 356 wavefields of Rayleigh wave at different in-plane propagation angles.

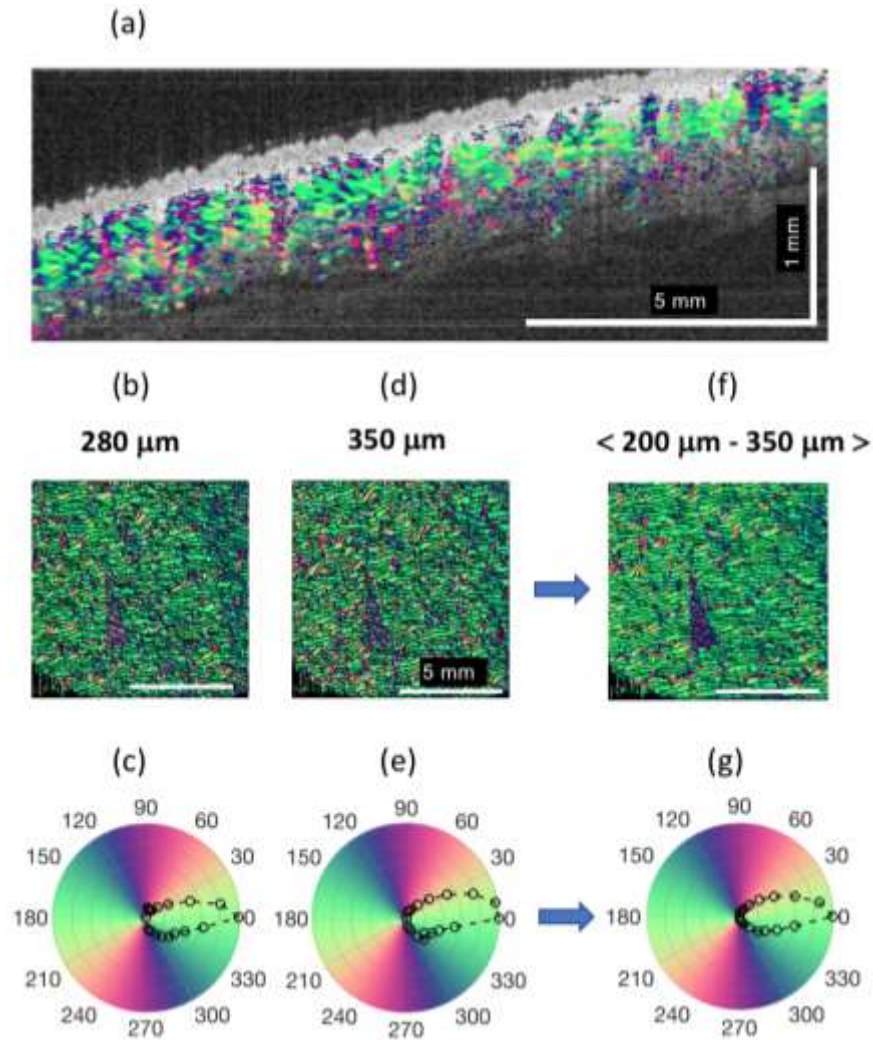
357 **Fiber orientation in skin: measurement with PS-OCT**

358 To determine whether measured mechanical anisotropy in skin correlates with its constituent
359 structure, the skin of each volunteer was also probed at the same sites with PS-OCT. We assume
360 that collagen fibers are the dominant birefringent scattering component in skin. Assuming that
361 the fibers define mechanical anisotropy, collagen fibers should also be anisotropic in orientation.
362 Fiber orientation and mechanical symmetry axes are not always well aligned, but alignment here
363 provides strong evidence that OCE data processing with the NITI model correctly defines
364 mechanical symmetry.

365 Polarization-sensitive optical coherence tomography (PS-OCT)^{51, 67-70}, an extension of
366 conventional optical coherence tomography (OCT), can characterize cross-sectional birefringent
367 biological structures non-invasively and can be used to determine the anisotropic orientation of
368 collagen fibers embedded within skin. In this study, the same forearm region scanned via OCE
369 was imaged using the PS-OCT system described in Refs.^{69,70} (see also details in the Methods
370 Section). This system provided depth-resolved axis orientation mapping of collagen fibers in the
371 skin up to a depth of $\sim 500 \mu\text{m}$.

372 Figure 3 presents collagen fiber directionality based on the depth-resolved apparent optic axis in
373 Subject #4. Non-birefringent components were removed using a color filter before computing
374 the axis orientation⁶⁸. The relative optic axis was mapped to a color-wheel where 0-degrees was
375 defined to align with the coordinate system in OCE. It is interesting (see Fig. 3a) that there is little
376 birefringence in a thin layer beneath the skin surface (up to a $100 \mu\text{m}$ depth) compared to deeper
377 skin tissue, suggesting poor collagen organization in the superficial layer. This thin layer
378 corresponds to the epidermis, which can be seen in the cross-sectional structure image. It is
379 uncolored in most points of the image (Fig. 3a), indicating that the epidermal layer does not
380 change the polarization state of the probing light beam. Hence, the epidermis is optically
381 minimally birefringent. Note that the epidermal layer is not captured by $\text{A}\mu\text{T-OCE}$ measurements
382 because it is very thin compared to the mechanical wavelength.

383 Although fibers are oriented differently in the dermis (see Fig. 3a), the preferred optic axis
384 orientation between $\sim 100 \mu\text{m}$ and $350 \mu\text{m}$ depth is quite clear (see Figs. 3 b-e for individual
385 layers, and the accumulated scattering anisotropy is seen in Figs. 3f,g). The accumulated
386 (averaged) optic axis orientation in the dermis can be compared with the orientation of the
387 mechanical axis obtained with $\text{A}\mu\text{T-OCE}$. Unfortunately, the sensitivity of the current PS-OCT
388 system is not enough to see if there is a preferred fiber orientation in subcutaneous tissue.



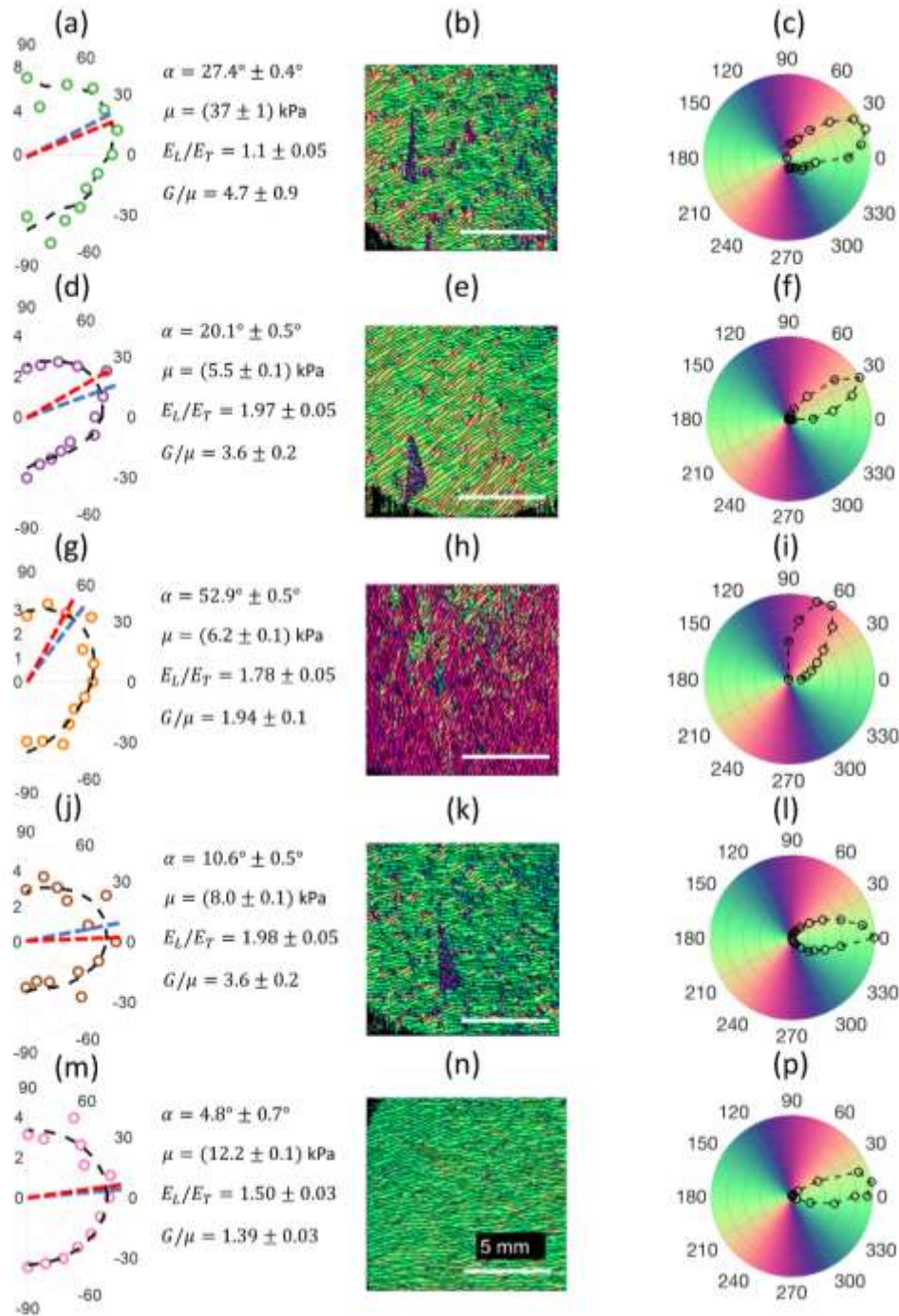
389

390 **Figure 3. Optical polarization maps in skin (forearm body area, Subject #4).** PS-OCT measurements were
 391 performed at the same body sites to compare with A μ T-OCE. **(a)**, Cross-section OCT image with the depth-
 392 resolved optic axis orientation measurement superimposed. **(b)**, **(d)**, **(f)** Color-encoded en-face slices (i.e.,
 393 C-Scan) of the apparent optic axis at different depths in skin (depths are shown at the top of panels), and
 394 **(c)**, **(e)**, **(g)** present in-plane optic axis patterns averaged over skin maps for the same depths. Last panels
 395 **(f)** and **(g)** are obtained by averaging of optic axis orientations over the entire depth in dermis. A piece of
 396 triangular black tape was used to align PS-OCT relative to A μ T-OCE measurements.

397

398 **Summary of anisotropy in skin of five healthy human subjects**

399 Measurements in skin in the forearm of five healthy human subjects were performed with both
 400 A μ T-OCE and PS-OCT methods. Data obtained for every subject were processed as described in
 401 the previous 2 sections. Results are summarized in Fig. 4.



402
 403 **Figure 4. Comparison of $A\mu T$ -OCE with PS-OCT measurements for all 5 human subjects.** Left column
 404 (panels (a), (d), (g), (j) and (m)) present $A\mu T$ -OCE measurements of mechanical anisotropy in skin in human
 405 forearm body sites in vivo. Central column (panels (b), (e), (h), (k) and (n)) show optic axis maps integrated
 406 over the dermis obtained with PS-OCT, and the right column (panels (c), (f), (i), (l) and (p)) shows
 407 directivity patterns of optical polarization in dermis integrated over the dermis thickness at the same body
 408 sites. Both methods reveal a similar symmetry direction for all human subjects. Blue and red dashed lines
 409 in the left column correspond to the skin's symmetry axis determined from $A\mu T$ -OCE and PS-OCT,
 410 respectively. A triangular piece of black tape helped align PS-OCT coordinates relative to $A\mu T$ -OCE
 411 measurements.

412 It is interesting, and encouraging, that the symmetry axes derived from optical and mechanical
413 measurements match very closely for all investigated subjects. In general, optical symmetry is
414 not always equal to the mechanical symmetry of a material. For human forearm skin, however,
415 it appears that optical and mechanical symmetry axes coincide.

416 As reported in the literature on Langer's lines in the forearm, the direction should be nearly
417 orthogonal to the axial forearm direction (α should be around zero). In our measurements, the
418 direction of Langer's lines was close to orthogonal in only 2 subjects (Subjects #4 and #5); in two
419 subjects, the inclination α was about 30°; and in one case α was about 60°.

420 An interesting observation can be found from the results shown in Fig.4. For four of five subjects
421 (subjects #2-#5), a higher value of shear anisotropy G/μ corresponds to higher tensile anisotropy
422 E_L/E_T . Both ratios depend on the relative density of fibers and their alignment in the measured
423 sites and may be functions of multiple physiological parameters. This observation is not
424 statistically significant but is the subject of a future study that will be performed in a much larger
425 population with subgroups of different body sites, age, sex, body mass index and other
426 parameters.

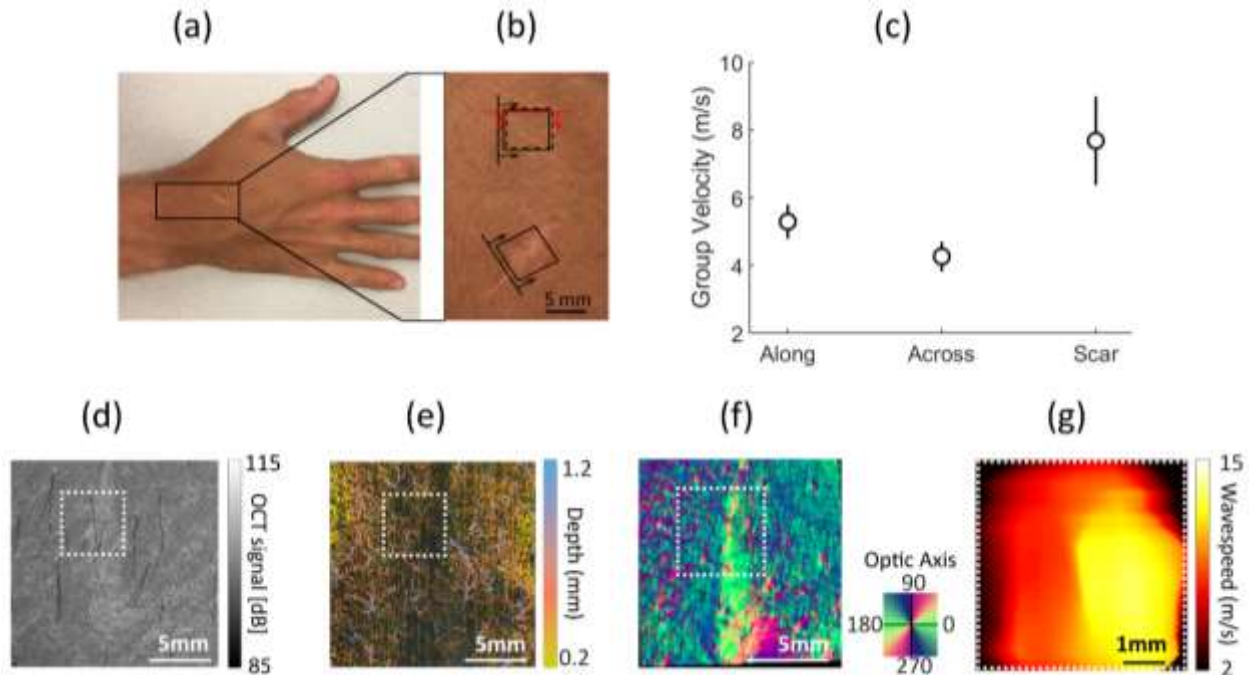
427 The fact that all elastic moduli (G , μ and δ) are much larger for subject #1 compared to other
428 subjects strongly imply that skin's elastic properties can vary greatly from person to person. This
429 suggests that personalized treatment plans are more likely required for both aesthetic and
430 reconstructive skin procedures.

431 **Imaging of scar in human wrist in vivo with multiple OCT modalities: preliminary results**

432 In recent decades, several optical diagnostic methods have been proposed to image skin and
433 evaluate scar. OCT is one of the most promising methods to provide diverse information on skin
434 constituents. Indeed, signal intensity in structural OCT images is driven by tissue scattering
435 properties, which are related to collagen density. OCT angiography (OCTa) can image
436 microvasculature. PS-OCT images skin's optical anisotropy by measuring optic (birefringence) axis
437 orientation, and OCE can image skin's elastic properties. Although individual OCT modalities were
438 used to compare normal skin structure and scar before, we do not know of any studies that have
439 demonstrated all four OCT modalities to characterize the same scar tissue. Here we present our
440 pilot results on imaging scarred skin with different OCT modalities and show that the information
441 obtained can be very rich, diverse and useful for clinicians to evaluate skin's state and function.

442 A 28 year old volunteer with a mature skin scar on the back of the hand (Fig. 5a,b) was imaged
443 using different OCT modalities in the area around the scar. The Rayleigh wave speed was
444 measured in the scar and compared with the wave speed in two orthogonal directions in normal
445 tissue around the scar. The x and y scanning directions each had 100 scan locations, spread across
446 a 6 mm x 6 mm scanning area. The wave speed was calculated using a moving kernel with 20
447 pixels. Overall, there were 80 different shear wave speed values (across x) by 100 values (across
448 y) used to determine the mean and variation in Figure 5c. As seen, the Rayleigh wave speed is
449 almost twice higher in scar tissue, providing evidence of the increased density of collagen fibers

450 in scar and with corresponding higher elastic moduli. This result is supported by the structural
 451 OCT image (Fig. 5d) where the scar area looks much brighter. The OCTa image (Fig. 5e) shows
 452 reduced density of capillaries, typical for certain types of mature scar tissue⁷¹. It can also be seen
 453 from the PS-OCT map (Fig. 5f) that the optic axis orientation is very different in scar compared to
 454 that of surrounding tissue. Finally, a 2D image of mechanical wave speed measured in the
 455 longitudinal direction in scar obtained with μ T-OCE is represented in Fig. 5g. It confirms very
 456 different mechanical properties of scar tissue with increased fiber content, and correlates well
 457 with the results of OCTa to demonstrate that mechanical properties of healed tissue cannot
 458 match those of surrounding areas without proper vascularization and collagen remodeling.



459
 460 **Figure 5. Characterization of scar tissue in vivo with four different OCT modalities.** (a) Photograph of the
 461 scar area in a 28-year-old male volunteer. (b) Its enlarged area with the direction of mechanical wave
 462 propagation in the scar and adjacent skin site. (c) Group velocity of Rayleigh wave in scar and in normal
 463 skin tissue in two orthogonal directions. Structural OCT (d) and OCTa (e) images obtained with the system
 464 described in Ref. ⁷². (f) Optic axis orientation map obtained with the PS-OCT system described in Ref. ⁶⁸.
 465 (g) Image of Rayleigh wave group velocity measured in the direction perpendicular to scar within the area
 466 covered by a white dashed rectangle (shown in panels (d)-(f) for scaling). The μ T-OCE image was
 467 obtained with the system described in Ref. ^{19, 64, 65}.

468 Discussion

469 There is no doubt that elasticity is intimately related to skin's aesthetics and function. Mapping
 470 skin's functional and mechanical properties is critical for reconstructive surgeries to restore both
 471 form and function while minimizing the impact of scar formation.

472 Although there are several commercial mechanical devices to measure skin's elastic properties,
 473 most use an inadequate, very simplified model of skin, cannot resolve spatial differences in

474 stiffness parameters, and have limited use in assessing burns, traumas, and grafts. Traditional
475 ultrasound elastography is also not appropriate because it requires mechanical contact to the
476 measurement site and faces difficulties in moduli inversion from experimental data due to skin's
477 layered structure.

478 Current aesthetic and reconstructive procedures do not include mapping and monitoring of skin
479 elasticity because there are no non-invasive devices providing quantitative maps of elastic
480 properties. Thus, there are no quantitative methods to longitudinally monitor the reconstruction
481 process and potentially generate feedback to help guide clinicians toward optimal outcomes and
482 inform the timing for future reconstructive procedures. Serial evaluations of pathologic scars
483 could also be used to document scar evolution over time and objectively measure improvements
484 from non-surgical scar interventions such as CO2 laser remodeling.

485 In this paper, we proposed A μ T-OCE (previously calibrated and tested for cornea) to map skin's
486 elastic moduli and anisotropy. The proposed method is non-contact and non-invasive. In
487 addition, OCT is already FDA approved for clinical use including surgical applications. Thus, there
488 is a clear, straightforward path to clinical translation of A μ T-OCE if it can be shown to be accurate
489 and efficient.

490 A μ T-OCE has other advantages beyond being non-contact. First, it can be very fast. Modern OCT
491 systems can scan a few million A-scans per second, which means OCE can be performed over a
492 soft tissue area of $\sim 1 \text{ cm}^2$ in less than a second. The method, therefore, can be used for on-line
493 monitoring and longitudinal diagnostics. Second, moduli inversion can be highly simplified in OCE
494 compared to traditional elastography because A μ T-OCE utilizes surface propagating waves. As
495 demonstrated in Results and Supplementary Notes 5,6, subcutaneous tissue may not greatly
496 affect wave propagation in dermis due to both the gradual transition from dermis to hypodermis
497 and the non-zero Young's modulus of deeper tissue. Thus, a bulk NITI material is appropriate to
498 reconstruct mechanical properties of the dermis from acoustic data. Third, all four OCT
499 modalities (structural OCT, OCTa, PS-OCT and OCE) deliver important information on skin shape,
500 structure, properties, and function. For example, skin thickness and its layered structure imaged
501 with OCT can be used to refine the mechanical model for OCE. Vascularization maps from OCTa
502 can be combined with skin's elasticity for better characterization of scar and skin during
503 reconstructive surgeries and aesthetic procedures. PS-OCT can help define skin's anisotropy and
504 differentiate lesions. It also delivers depth-resolved anisotropy, which is not currently
505 demonstrated with OCE. Although we used different OCT setups to image skin with different OCT
506 modalities, all four can be combined into a single device.

507 In our study, we used a NITI model to characterize the mechanical properties of skin. Although
508 skin consists of 3 sequential layers, the epidermis functions mainly as a protective outer layer
509 and does not greatly influence skin elasticity⁵⁴. On the other hand, hypodermis mostly connects
510 outer skin layers with internal structures and provides thermal insulation. Its elasticity is much
511 smaller than that in dermis and, thus, dermis mainly defines skin mechanical properties. As
512 discussed above, we showed that the Rayleigh wave speed used to reconstruct the Young's
513 modulus is mainly defined by the elastic properties of dermis. The thin epidermis is much smaller

514 than the wavelength of propagating waves and does not significantly affect Rayleigh wave
515 propagation. The results of fits to theoretical functions (see left column in Fig. 4) confirm that the
516 NITI model well describes the anisotropy in dermis, even though the Rayleigh wave speed for in-
517 plane anisotropy has a complicated shape. Finally, PS-OCT provided independent confirmation
518 that the NITI model is appropriate for skin since the primary fiber orientation in dermis as
519 measured by PS-OCT is very close to that obtained with A μ T-OCE (see Fig. 4).

520 Although the results presented here on skin's elasticity and its anisotropy in the human forearm
521 are promising, future studies are clearly needed to validate its diagnostic value. Our studies here
522 were limited to imaging forearm sites and acquiring pilot measurements in scar. We have not
523 performed detailed studies of skin at other anatomical sites where its mechanical properties may
524 be substantially different. For example, at sites in the face, and other areas where large blood
525 vessels, bones or cartilages are located close to the skin surface, additional model refinement
526 may be required. In addition, as PS-OCT images show (see Figs. 3,4) in five volunteers, skin sites
527 in the forearm have a primary fiber orientation; however, it is not clear that skin at an arbitrary
528 body site can be considered a NITI material. Thus, independent co-measurement of tissue
529 anisotropy with PS-OCT, for example, or with any other method is desirable for all A μ T-OCE
530 studies. As shown in Fig. 5, the combination of different OCT modalities would be ideal because
531 they can deliver very diverse information on skin's structure (vascularization, skin layers'
532 thickness, in-depth distribution of optical anisotropy). All these parameters may help refine skin's
533 local biomechanical model and make reconstructing mechanical moduli more accurate and
534 reliable.

535 In our NITI model (see Supplementary Notes 1-3), we ignored viscosity, which might influence
536 reconstruction accuracy and require additional corrections. We observed that mechanical waves
537 can propagate for more than 10 wavelengths over the skin surface for the anatomical sites
538 studied and, therefore, viscosity is not very strong and does not significantly affect the
539 propagation speed. If, indeed, guided waves are not excited in skin because of the smooth
540 transition in elastic properties at the dermis/hypodermis interface, and the main mode is a
541 Rayleigh wave, then skin's viscosity can be determined from the wave attenuation⁷³. This will be
542 a subject of future work.

543 In future human subject studies, we will obtain baseline elastic properties of skin at different
544 anatomical sites in volunteers of different age, gender, race, and body mass index. This
545 information will be vital to define the normal range of variations in skin elastic properties and
546 their influence on its aesthetics and function. In additional studies, we will monitor skin graft
547 procedures at all steps starting from initial mapping of skin's elasticity in donor and recipient sites
548 preoperatively, perioperatively, and postoperatively through the sequential wound healing
549 phases of inflammation, proliferation, and remodeling. We anticipate that a quantitative
550 elasticity mapping tool appropriate for the clinic will dramatically improve skin reconstructive
551 procedures by minimizing scars and optimizing outcomes. Similarly, we hope to show that
552 longitudinal volumetric mapping of skin elasticity can reduce graft failure and secondary
553 contracture at the recipient site and limit the need for revisionary surgery. We also hope that
554 A μ T-OCE can be utilized in future clinical studies to quantify the biomechanical function and

555 aesthetic parameters of existing surgical procedures and aid in the development of new protocols
556 for novel skin surgeries.

557 Mapping skin elasticity with sub-mm resolution is not limited to skin grafting only. It may
558 significantly impact cosmetics, dermatology, transplantology and plastic surgery, dramatically
559 improving current monitoring of wound healing and tissue recovery, reducing surgical failure
560 rates, providing immediate quantitative feedback on all procedures, and opening many new
561 opportunities for reconstructive medicine.

562 **Methods**

563 **Analytic model**

564 Based on the presence of Langer's lines defining the primary orientation of collagen fibers in skin,
565 a NITI model was proposed to describe its elastic properties. As demonstrated in Results and in
566 Supplementary Notes 4,5, Rayleigh wave propagation in skin does not need to explicitly account
567 for its layered structure, i.e. Rayleigh waves on the skin surface can be described as surface waves
568 on a bulk NITI material (see Supplementary Notes 3). Propagation of bulk and Rayleigh
569 mechanical waves are considered in Supplementary Notes 2 and 3, respectively.

570 **Numerical simulation**

571 As noted above, the bulk NITI model was used to describe the Rayleigh wave propagation over
572 the skin surface. To study how a thin layer (epidermis) on the top of the NITI medium affects
573 wave propagation, as well as how subcutaneous tissue influences guided wave behavior in
574 dermis, numerical simulations were performed. We developed a finite element numerical model
575 for both cases using OnScale (OnScale, Redwood City, CA). A full description of the simulation
576 results is provided in Supplementary Notes 4 and 5.

577 The computational domain was discretized using linear finite elements on a regular rectangular
578 grid with at least 40 elements per elastic wavelength. Simulations were solved using explicit time
579 stepping, and the vertical velocity component was extracted for analysis, similar to OCE
580 experiments where only this component is available.

581 OnScale scripts for the simulation of Rayleigh wave propagation in 2-layer (epidermis/dermis)
582 and 3-layer (epidermis/dermis/subcutaneous tissue), as well as the corresponding Matlab scripts
583 to compute and plot wavefields and 2D Fourier spectra of Rayleigh waves are provided in
584 Supplementary Software Library.

585 Matlab scripts to calculate wave velocities of bulk and Rayleigh waves in YZ plane of a fast-axis
586 NITI material for different parameters μ , G , and δ are provided in Supplementary Software
587 Library.

588

589 **A μ T-OCE imaging system and measurement**

590 To generate elastic waves without any contact to the skin surface, we applied an excitation push
591 with acoustic micro-tapping (A μ T), a technique using a cylindrically focused, air-coupled
592 ultrasound transducer to induce a localized radiation force at the tissue surface^{18-21, 64, 65}. The
593 A μ T transducer effectively applied a line load to the surface over a wide region relative to the
594 propagation distance of interest, resulting in approximately planar elastic waves (normal to the
595 OCT imaging plane).

596 Mechanical waves propagating over the skin surface were detected using a phase-sensitive
597 frequency-domain OCT (PhS-OCT) system (see Fig. 6a), which has been described in previous
598 studies^{20, 64, 65}. The sampling rate of the 1024-pixel line-scan InGaAs array was set to 46.5 kHz,
599 determining the A-line rate of the system (temporal resolution). The optical resolution was
600 approximately 15 μ m axially and 24 μ m laterally. An external TTL trigger synchronized the PhS-
601 OCT system with wave excitation for each M-scan. All data were collected in M-B format in which
602 512 A-scans are repeated in the same location (M-scan) at 256 different horizontal locations (B-
603 scan) across the imaging plane ($dx = 54.7 \mu$ m), forming a complete M-B scan (1024 depth \times 256
604 lateral locations \times 512 temporal frames) with an effective imaging range of 1.5 mm \times 10 mm
605 (axial \times lateral). One full M-B scan took 3.66 s.

606 To measure the angle-dependent surface wave speed, the imaging arm (consisting of galvo
607 mirror, focusing lens, and A μ T transducer) was mounted on a rotational stage with the axis of
608 rotation located in the center of the OCT FOV (Fig. 6b). The rotational stage was equipped with
609 an adjustable screw that allowed for fine-angle rotations over a range of 180 degrees. The entire
610 imaging arm was rotated 15 degrees at a time to measure wave propagation along different
611 directions. A 20 mm wide rigid circular ring was mounted near the co-aligned OCT and A μ T focus
612 to ensure easy forearm alignment and limit bulk motion.

620 **Reconstruction of Young's modulus and elastic anisotropy in skin**

621 μ T-OCE recorded Rayleigh wavefields (see Figs. 2c-i) propagating over the skin surface at
622 different orientations relative to the longitudinal forearm direction. Linear fits were applied to
623 all wavefields to obtain the group velocity of propagating waves. Wave velocities measured at
624 different propagation directions created the anisotropy map of surface wave speed.

625 Ideally, to reconstruct elastic moduli, an analytic solution for the Rayleigh wave equation should
626 be used. Unfortunately, obtaining an analytic form of the Rayleigh wave equation in the NITI
627 medium is possible only along the primary symmetry axes⁷⁴ (see Supplementary Note 3), which
628 is not sufficient to reconstruct all 3 constants.

629 Instead, experimentally obtained wave speed anisotropy maps were fit with numerically
630 obtained functions of Rayleigh wave anisotropy in the NITI model. Fitting was performed with
631 four parameters: G , μ and δ and fiber orientation α . The last had an original guess corresponding
632 to the results obtained with the PS-OCT for the fiber orientation in dermis. The accuracy of
633 reconstruction and its sensitivity to experimental data variation was determined by a 'Leave-one-
634 out cross-validation' method⁶⁶. An example of fitting results is presented in Fig. 2b; summary of
635 data fitting for all human subjects is shown in Fig. 4.

636 **PS-OCT imaging system and measurement**

637 The PS-OCT system^{69, 70} used a 100-kHz MEMS-VCSEL swept laser source (SL1310V1-20048,
638 Thorlabs), providing an output power of 25 mW with a central wavelength of 1310 nm and a
639 spectral tuning range of 100 nm. The source output was sent to a polarization controller and
640 linearly polarized through a polarization beam splitter and then split into reference and sample
641 arms through an additional beam splitter at a split-ratio of 50:50. The sample arm was equipped
642 with a quarter wave plate (QWP) aligned at 45° with respect to the input polarization state,
643 resulting in a circularly polarized light incident at the sample surface. Light coming back from
644 both reference and sample arms were recombined so that interfering light was split into
645 horizontal and vertical polarization components. Balanced detection was used for both channels
646 to collect the interference signals, from which PS-OCT images are reconstructed. In this system,
647 PS-OCT was performed with the objective lens (LSM03, Thorlabs Inc., U.S.), providing a lateral
648 resolution of 30 μ m. The axial resolution was approximately 7.5 μ m, in air.

649 The FOV was 11 mm x 11 mm centered over the OCE region marked with ink. To improve SNR,
650 four repeat B-scans were performed at each location and interference signals averaged prior to
651 processing. Entire volumetric scanning, consisting of 500 A-lines in the y-axis direction and 2000
652 A-lines in the x-axis direction, took 13.2 s.

653 **Reconstruction of depth-resolved orientation of optic polarization axis in skin**

654 A polarization state tracing (PST) method was used to derive the depth-resolved phase
655 retardation and axis orientation from PS-OCT measurements⁷⁰. In this approach, output

656 polarization states were represented by the Stokes parameters⁶⁸. Before depth-resolved phase
657 retardation and axis orientation were calculated, a color filter was applied to remove the
658 amorphous tissue at the surface that does not alter input polarization⁶⁸. A sliding window
659 containing 3 adjacent output polarization states along depth was used to do local plane fitting
660 progressively using singular value decomposition. Then, the normal vector of each local fitting
661 plane is obtained and utilized to determine the final spatially resolved orientation of the optic
662 polarization axis⁷⁰.

663 **OCT/OCTa imaging system and measurement**

664 The swept-source OCT (SS-OCT) system employed in this study has been previously reported in
665 detail⁷⁵. Briefly, a 200-kHz vertical-cavity surface-emitting (VCSEL) swept laser source
666 (SL1310V1–10048, Thorlabs Inc., Newton, NJ) with a central wavelength of 1305 nm (spectral
667 tuning range of 100 nm) was utilized, providing an axial resolution of ~8 μm in tissue (~11 μm in
668 air). The imaging arm was attached to a hand-held probe via shielded optical cables and an 18 mm
669 effective focal length lens (LSM02, Thorlabs Inc.) was used to provide a lateral resolution of ~10
670 μm . A glass coverslip was attached to ensure the OCT focal plane was aligned with the epidermal-
671 dermal junction and provide stability during imaging. A small amount of glycerol was applied to
672 the skin to remove air gaps between the glass and skin.

673 3D volumetric scans were acquired with a field of view (FOV) of 10 mm \times 10 mm. The beam spot
674 was scanned using a paired X-Y galvo scanner (6210H, Cambridge Technology, Bedford, MA),
675 forming raster sampling patterns comprising fast (x-axis) and slow (y-axis) scans. At each y-
676 location, 800 A-scans were acquired to create a single B-frame. Eight B-frames were repeated
677 before moving to the next y-location to improve SNR. Following this protocol, a single 3D
678 volumetric scan (C-scan) was generated (a detailed analysis of a typical OMAG scan sequence
679 was previously reported by Deegan, *et al.*⁷²).

680 Repeated frames were used to generate the optical microangiography (OMAG) image based on
681 eigen decomposition (ED) analysis⁷⁶. This technique uses repeated B-frames to provide a 3D
682 volume image contrasted by particles in motion. The scan protocol was designed to contrast
683 capillary vessels based on red blood cell scattering, providing 3D contrast of vascular structure.
684 The method resulted in a co-registered image of both static (tissue) and dynamic (RBC)
685 components providing information on both local tissue and vascular structure. For visualization,
686 3D data were compressed to maximum intensity projected en-face vascular images, with the ED-
687 signal above a 5 dB threshold displayed and mapped to a color based on depth⁷². 3D data were
688 cropped approximately 450 μm below the tissue surface to limit the noise-contribution from light
689 attenuation.

690 **Human subjects**

691 The study was performed in accordance with University of Washington policies and regulation
692 applied to the studies involving human subjects and approved by the University of Washington
693 Institutional Review Board (IRB) (STUDY00012306). University of Washington IRB was established

694 in accordance with the federal regulations for protecting the rights and welfare of human
695 research subjects. For all volunteers who participated in this study, informed consent was
696 obtained from all subjects.

697 Five healthy volunteers between 28 and 32 years old (2 male, 3 female), nonsmokers without
698 known skin conditions and diseases, were scanned in vivo with both A μ T-OCE and PS-OCT
699 systems in the forearm area. A small piece of black tape was attached to the subjects' skin to
700 align both A μ T-OCE and PS-OCT measurements. A black felt-tip marker highlighted the ROI used
701 in both OCE and PS-OCT.

702 Additional measurements with four different OCT modalities (structural OCT, OCTa, A μ T-OCE and
703 PS-OCT) were performed around scar tissue located on the back of the hand of a 28-year-old
704 male volunteer. The mature scar tissue formed during the healing process of a deep incision
705 wound. The wound was allowed to heal naturally (no sutures) resulting in a ~11 mm long by ~4
706 mm wide region of scar tissue. An imaging window was carefully cleared using a shaving razor 24
707 hours prior to imaging.

708 A μ T-OCE and PS-OCT measurements were performed in vivo without mechanical contact or any
709 skin preparations to subjects. Structural OCT and OCTa utilized a glass coverslip to reduce motion
710 artifact but can be performed without contact following small system modification.

711 **Acknowledgements**

712 This work was supported, in part, by NIH grants R01-AR077560-01, R01-EY026532, R01-
713 EY024158, R01-EB016034, R01-CA170734, and R01-HL093140, Life Sciences Discovery Fund
714 3292512, the Coulter Translational Research Partnership Program, an unrestricted grant from the
715 Research to Prevent Blindness, Inc., New York, and the Department of Bioengineering at the
716 University of Washington. M. Kirby was supported by NSF graduate fellowship (No. DGE-
717 1256082). Authors also thank the group of Professor Katherine Nightingale from Duke University
718 for a very useful discussion about mechanical models of anisotropic biological tissues. We also
719 acknowledge Kit Hendrickson for some help in illustrating Figure 6.

720 **Data Availability**

721 The authors declare that all data from this study are available within the Article and its
722 Supplementary Information. Raw data for the individual measurements are available on
723 reasonable request.

724 **Author Information**

725 **Affiliations**

726 Department of Bioengineering, University of Washington, Seattle, WA, USA

727 Mitchell A. Kirby, Peijun Tang, Maju Kuriakose, Hong-Cin Liou, John J. Pitre Jr., Ruikang K. Wang,
728 Matthew O'Donnell & Ivan Pelivanov

729 Harborview Medical Center, University of Washington, Seattle, WA, USA
730 Tam N. Pham, Russell Ettinger

731 **Contributions**

732 M.A.K. conducted A μ T-OCE and OCT/OCTa experiments, processed experimental data, analyzed
733 experimental results, and wrote the paper.

734 P.T. conducted PS-OCT measurements, processed experimental data, analyzed PS-OCT results,
735 and wrote the paper.

736 M.K. developed algorithms to reconstruct elastic moduli in skin by anisotropy of Rayleigh wave
737 speed; performed numerical simulations; processed A μ T-OCE results.

738 H.-C.L. developed algorithms to reconstruct elastic moduli in skin by anisotropy of Rayleigh wave
739 speed; performed numerical simulations; processed A μ T-OCE results.

740 J.J.P. developed the NITI model to characterize skin's elasticity; performed analytical studies;
741 designed a finite element model (FEM) to simulate mechanical waves in skin accounting for its
742 anisotropy, finite thickness, and boundary conditions; ran numerical simulations; developed
743 algorithms to reconstruct elastic moduli in skin base on the anisotropy of Rayleigh wave speed.

744 R.K.W. designed the study; developed the OCTa and PS-OCT systems used in this study;
745 performed analytical studies; wrote the paper.

746 M.O.D. designed the study, developed the NITI model to characterize skin's elasticity; wrote the
747 paper.

748 T.P. helped design in vivo studies and analyze obtained results, wrote the paper.

749 R.E. helped design in vivo studies and analyze obtained results, wrote the paper.

750 I.P. conceived the idea of using the NITI model in skin; designed and managed the study;
751 developed the NITI model to characterize skin's elasticity; performed analytical studies; and
752 wrote the paper.

753 **Corresponding author**

754 Correspondence to Ivan Pelivanov: ivanp3@uw.edu.

755 **Ethics Declarations**

756 **Competing interests**

757 The authors declare no competing interests.

758 **References**

- 759
- 760 1. Xu, F., Lu, T. J., Seffen, K. A. Thermally-induced change in the relaxation behavior of skin
761 tissue. *J. Biomech. Eng.* **131**(7), 071001 (2009).
- 762 2. Zhou, B., Xu, F., Chen, C. Q., Lu, T. J. Strain rate sensitivity of skin tissue under
763 thermomechanical loading. *Phil. R. Soc. A* **368**(1912), 679-690 (2010).
- 764 3. Escoffier, C. *et al.* Age-related mechanical properties of human skin: An *in vivo* study. *J.*
765 *Invest. Dermatol.* **93**, 353–357 (1989).
- 766 4. Boyer, G. *et al.* Non contact method for in vivo assessment of skin mechanical properties
767 for assessing effect of ageing. *Med. Eng. Phys.* **34**(2), 172-178 (2012).
- 768 5. Wei, J.C.J. *et al.* Allometric scaling of skin thickness, elasticity, viscoelasticity to mass for
769 micro-medical device translation: from mice, rats, rabbits, pigs to humans. *Sci. Rep.* **7**,
770 15885 (2017).
- 771 6. Joodaki, H., Panzer, M. B. Skin mechanical properties and modeling: A review. *Proc. Inst.*
772 *Mech. Eng. H* **232**(4), 323-343 (2018).
- 773 7. Tilleman, T. R., Tilleman, M. M., Neumann, M. The elastic properties of cancerous skin:
774 Poisson's ratio and Young's modulus. *Isr. Med. Assoc. J.* **6**, 753–755 (2004).
- 775 8. [https://www.plasticsurgery.org/documents/News/Statistics/2018/plastic-surgery-](https://www.plasticsurgery.org/documents/News/Statistics/2018/plastic-surgery-statistics-full-report-2018.pdf)
776 [statistics-full-report-2018.pdf](https://www.plasticsurgery.org/documents/News/Statistics/2018/plastic-surgery-statistics-full-report-2018.pdf)
- 777 9. Hallock, G. G. The skin graft. *Contemp. Surg.* **25**, 46-48 (1984).
- 778 10. Shimizu, R., Kishi, K. Skin grafts. *Plast. Surg. Int.* **2012**, 563493 (2012).
- 779 11. Hallock, G. G., Morris, S. F. Skin grafts and local flaps. *Plast. Reconstr. Surg.* **127**(1), 5e-22e
780 (2011).
- 781 12. Cheng, C. *et al.* Cell-assisted skin grafting: improving texture and elasticity of skin grafts
782 through autologous cell transplantation. *Plast. Reconstr. Surg.* **137**(1), 58e-66e (2016).
- 783 13. Min, J. H. *et al.* The use of Matriderm and autologous skin graft in the treatment of full
784 thickness skin defects. *Arch. Plast. Surg.* **41**(4), 330–336 (2014).
- 785 14. Langer, K. On the anatomy and physiology of the skin. *Brit. J. Plast. Surg.* **31**(1), 3–8
786 (1978).
- 787 15. Fore, J. A review of skin and the effects of aging on skin structure and function. *Ostomy*
788 *Wound Manage* **52**(9), 24-35 (2006).
- 789 16. Rosado, C. *et al.* About the in vivo quantification of skin anisotropy. *Skin Res. Technol.*
790 **23**(3), 429-436 (2017).
- 791 17. Larin, K. V., Sampson, D. D. Optical coherence elastography – OCT at work in tissue
792 biomechanics. *Biomed. Opt. Express* **8**, 1172-1202 (2017).
- 793 18. Ambroziński, Ł. *et al.* Air-coupled acoustic radiation force for non-contact generation of
794 broadband mechanical waves in soft media. *Appl. Phys. Lett.* **109**, 043701 (2016).

- 795 19. Ambroziński Ł. *et al.* Acoustic micro-tapping for non-contact 4D imaging of tissue elasticity,
796 *Sci. Rep.* **6**, 38967 (2016).
- 797 20. Pitre, J. J. *et al.* Nearly-incompressible transverse isotropy (NITI) of cornea elasticity: model
798 and experiments with acoustic micro-tapping OCE. *Sci. Rep.* **10**, 12983 (2020).
- 799 21. Kirby, M.A. *et al.* Delineating corneal elastic anisotropy in a porcine model using non-
800 contact optical coherence elastography and ex vivo mechanical tests. *Ophthalmology*
801 *Science*, (2021) (in press).
- 802 22. Edwards. C., Marks. R. Evaluation of biomechanical properties of human skin. *Clin.*
803 *Dermatol.* **13**(4), 375-80 (1995).
- 804 23. Benitez, J. M., Montans, F. J. The mechanical behaviour of skin: structures and models for
805 the finite element analysis. *Computers and Structures* **190**, 75–107 (2017).
- 806 24. Kang, M. J., Kim, B.-S., Hwang, S., Yoo, H. H. Experimentally derived viscoelastic properties
807 of human skin and muscle in vitro. *Medical Engineering & Physics* **61**, 25-31, (2018).
- 808 25. Pawlaczyk. M., Lelonkiewicz. M., Wieczorowski. M. Age dependent biomechanical
809 properties of the skin. *Postepy Dermatol. Alergol.* **30**(5), 302–306 (2013).
- 810 26. Diridollou S. *et al.* Skin ageing: changes of physical properties of human skin in vivo. *Int. J.*
811 *Cosmet. Sci.* **23**(6), 353-62 (2001).
- 812 27. Jemec, G. B., Gniadecka, M., Jemec, B. Measurement of skin mechanics: A study of inter-
813 and intra-individual variation using the Dermaflex A. *Skin. Res. Technol.* **2**(4), 164-166
814 (1996).
- 815 28. Sin, P., Stupka, I., Brychta, P. Evaluation and comparison of composite and split-thickness
816 skin grafts using cutometer mpa 580. *Ann. Burns. Fire Disasters;* **23**(4), 208–213. (2010).
- 817 29. Karla, A., Lowe, A., Al-Jumally, A. M. Mechanical behavior of skin: a review. *J. Material Sci.*
818 *Eng.* **5**(4). 1000254 (2016).
- 819 30. Zheng, Y., Mak, A. F. T. Effective elastic properties for lower limb soft tissues from manual
820 indentation experiment. *IEEE Tran. Rehab. Eng.* **7**(3), 257-267 (1999).
- 821 31. Boyer, G. *et al.* Dynamic indentation on human skin in vivo: ageing effects. *Skin. Res.*
822 *Technol.* **15**(1), 55-67 (2009).
- 823 32. Boyer, G. *et al.* In vivo characterization of viscoelastic properties of human skin using
824 dynamic micro-indentation. *Proc. 29th Annual International Conference of the IEEE*
825 *Engineering in Medicine and Biology Society.* 4584-4587 (2007).
- 826 33. Crichton, M. L. *et al.* Elastic modulus and viscoelastic properties of full thickness skin
827 characterized at micro scales. *Biomaterials* **34**(8), 2087-2097 (2013).
- 828 34. Hendriks, F. M. *et al.* A numerical-experimental method to characterize the non-linear
829 mechanical behavior of human skin. *Skin. Res. Technol.* **9**(3), 274-283 (2003).
- 830 35. Diridollou, S. *et al.* In vivo model of the mechanical properties of the human skin under
831 suction. *Skin Res. Technol.* **6**(4), 214-221 (2000).
- 832 36. Liang, X., Boppart, S. A. Biomechanical properties of in vivo human skin from dynamic
833 optical coherence elastography. *IEEE Tran. Biomed. Eng.* **57**, 953-959 (2010).

- 834 37. Sanders, R. Torsional elasticity of human skin in vivo. *Pflugers Arch.* **342**(3), 255-601 (1973).
- 835 38. Agache, P. G. *et al.* Mechanical properties and Young's modulus of human skin in vivo. *Arch.*
836 *Dermatol. Res.* **269**(3), 221-232 (1980).
- 837 39. Ankersen J *et al.* Puncture resistance and tensile strength of skin simulants. *Proc. Inst. Mech.*
838 *Eng. H* **213**(6), 493-501 (1999).
- 839 40. Jacquemoud, C., Bruyere-Garnier, K., Coret, M. Methodology to determine failure
840 characteristics of planar soft tissues using a dynamic tensile test. *J. Biomech.* **40**(2), 468-75
841 (2007).
- 842 41. Ottenio, M. *et al.* Strain rate and anisotropy effects on the tensile failure characteristics of
843 human skin. *J. Mech. Behav. Biomed. Mater.* **41**, 241-50 (2015).
- 844 42. Fearmonti, R., Bond, J., Erdmann, D., Levinson, H. A review of scar scales and scar measuring
845 devices. *Eplasty.* **10**, e43 (2010).
- 846 43. Sigrist, R. M. S. *et al.* Ultrasound elastography: review of techniques and clinical
847 applications. *Theranostics* **7**(5), 1303-1329 (2017).
- 848 44. Sarvazyan, A. P. *et al.* Shear wave elasticity imaging: a new ultrasonic technology of medical
849 diagnostics. *Ultrasound in Med. Biol.* **24**, 1419–1435 (1998).
- 850 45. Gennisson, J. L. *et al.* Ultrasound elastography: principles and techniques. *Diagn. Interv.*
851 *Imaging* **94**(5), 487-95 (2013).
- 852 46. Ferraioli, G. *et al.* Liver Ultrasound Elastography: An Update to the World Federation for
853 Ultrasound in Medicine and Biology Guidelines and Recommendations. *Ultrasound Med.*
854 *Biol.* **44**(12), 2419-2440 (2018).
- 855 47. Barr, R. G. Future of breast elastography. *Ultrasonography.* **38**(2), 93-105. (2019).
- 856 48. O'Donnell, M., Skovoroda, A.R. Prospects for elasticity reconstruction in the heart. *IEEE*
857 *Tran. UFFC* **51**(3), 322-328 (2004).
- 858 49. Lakhani, P., Dwivedi, K.K., Kumar, N. Directional dependent variation in mechanical
859 properties of planar anisotropic porcine skin tissue. *J. Mech. Behav. Biomed. Mater.* **104**,
860 103693 (2020).
- 861 50. Ní Annaidh, A. *et al.* Characterization of the anisotropic mechanical properties of excised
862 human skin. *J Mech Behav Biomed Mater.* **5**(1), 139-148. (2012).
- 863 51. de Boer, J. F., Hitzengerger, C. K., Yasuno, Y. Polarization sensitive optical coherence
864 tomography - a review. *Biomed Opt. Express* **8**(3), 1838-1873 (2017).
- 865 52. Pailler-Mattei, C. *et al.* In vivo skin biophysical behavior and surface topography as a
866 function of ageing. *J. Mech. Behav. Biomed. Mater.* **28**, 474-483 (2013).
- 867 53. Karla, A., Lowe, A. An overview of factors affecting the skins Young's modulus. *J. Aging Sci.*
868 **4**(2), 1000156 (2016).
- 869 54. Carroll, R.G. *Elsevier's Integrated Physiology.* (Elsevier, 2007).

- 870 55. Rouze, N.C. *et al.* Finite element modeling of impulsive excitation and shear wave
871 propagation in an incompressible, transversely isotropic medium. *J. Biomech.* **46**(16), 2761-
872 2768 (2013).
- 873 56. Rouze, N. C., Palmeri, M. L, Nightingale, K. R. Tractable calculation of the Green's tensor for
874 shear wave propagation in an incompressible, transversely isotropic material. *Phys. Med.*
875 *Biol.* **65**(1), 015014 (2020).
- 876 57. Xiang, X. *et al.* Quantitative assessment of healthy skin elasticity: reliability and feasibility
877 of shear wave elastography. *Ultrasound Med. Biol.* **43**(2), 445-452 (2017).
- 878 58. Yang, Y. *et al.* Quantification of skin stiffness in patients with systemic sclerosis using real-
879 time shear wave elastography: a preliminary study. *Clin. Exp. Rheumatol.* **36**(4) Suppl. 113,
880 118-125 (2018).
- 881 59. Tang, Y. *et al.* Quantification of skin lesions using high-frequency ultrasound and shear wave
882 elastography in port-wine stain patients: a clinical study. *Ann. Transl. Med.* **7**(24), 803
883 (2019).
- 884 60. Vexler, A., Polyansky, I., Gorodetsky, R. Evaluation of skin viscoelasticity and anisotropy by
885 measurement of speed of shear wave propagation with viscoelasticity skin analyzer. *J Invest*
886 *Dermatol.* **113**(5), 732-739 (1999).
- 887 61. Tanuma, K. Stroh formalism and Rayleigh waves. *J. Elasticity* **89**, 5–154 (2007).
- 888 62. Cherry, M. R., Sathish, S. & Grandhi, R. A numerical method for predicting Rayleigh surface
889 wave velocity in anisotropic crystals. *J. Comput. Phys.* **351**, 108–120 (2017).
- 890 63. Abramowitz, M., Stegun, I. A. Handbook of Mathematical Functions (Dover, NY, 1970).
- 891 64. Kirby, M.A. *et al.* Optical coherence elastography in ophthalmology. *J. Biomed. Opt.*
892 **22**(12), 1-28 (2017).
- 893 65. Kirby, M.A. *et al.* Spatial resolution in dynamic optical coherence elastography. *J. Biomed.*
894 *Opt.* **24**(9), 096006. (2019).
- 895 66. Molinaro, A. M., Simon, R., Pfeiffer, R. M. Prediction error estimation: a comparison of
896 resampling methods. *Bioinformatics* **21**(15), 3301-3307 (2005).
- 897 67. Fan, C., Wang, Y., Wang, R. K. Spectral domain polarization sensitive optical coherence
898 tomography achieved by single camera detection. *Opt. Express* **15**(13), 7950-7961 (2007).
- 899 68. Tang, P., Xu, J., Wang, R. K. Imaging and visualization of the polarization state of the probing
900 beam in polarization-sensitive optical coherence tomography. *Appl. Phys. Lett.* **113**, 231101
901 (2018).
- 902 69. Tang, P., Wang R. K. Polarization sensitive optical coherence tomography for imaging
903 microvascular information within living tissue without polarization-induced
904 artifacts. *Biomed. Opt. Express* **11**(11), 6379-6388 (2020).
- 905 70. Tang, P., Wang R. K. Polarization state tracing method to map local birefringent properties
906 in samples using polarization sensitive optical coherence tomography. *Biomed. Opt. Express*
907 **11**(12), 6852-6863 (2020).

- 908 71. Deegan, A. J., *et al.* Optical coherence tomography angiography of normal skin and
909 inflammatory dermatologic conditions. *Lasers Surg. Med.* **50**(3), 183-193 (2018).
- 910 72. Viktorov, I. A. Rayleigh and Lamb waves: physical theory and applications. (Plenum press,
911 1970).
- 912 73. Song, S. *et al.* Robust numerical phase stabilization for long-range swept-source optical
913 coherence tomography. *J. Biophotonics* **10**(11), 1398-1410 (2017).
- 914 74. Destrade, M. Surface waves in orthotropic incompressible materials. *JASA* **110**(2), 837-840
915 (2001).
- 916 75. Wang, R. K. *et al.* Optical coherence tomography angiography-based capillary velocimetry.
917 *Journal Biomed. Opt.* **22**(6), 066008 (2017).
- 918 76. Beer, T. W. *et al.* Angiogenesis in pathological and surgical scars. *Hum. Pathol.* **29**(11), 1273-
919 1278 (1998).

Supplementary Files

This is a list of supplementary files associated with this preprint. Click to download.

- [PelivanovSupplementaryskinSciRepsubmission.pdf](#)
- [SupplementarySoftwareLibrary.zip](#)